PCCP

ROYAL SOCIETY OF CHEMISTRY

PAPER

View Article Online
View Journal | View Issue



Cite this: *Phys. Chem. Chem. Phys.*, 2023, **25**, 1987

# Thermoelectric properties and lattice dynamics of tetragonal topological semimetal $Ba_3Si_4$

Romain Viennois, *[a] Michael Marek Koza,[b] Adrien Moll [ac] and Mickael Beaudhuin [a]

Received 4th October 2022,
Accepted 6th December 2022

DOI: 10.1039/d2cp04631h

rsc.li/pccp

We report the lattice dynamics and thermoelectric properties of topological semimetal $Ba_3Si_4$. The lattice dynamics has been studied by Raman and inelastic neutron scattering experiments. Good agreement has been found with first-principles calculations. The presence of low-energy optical modes at about 7 meV mainly due to the heavy mass of the Ba atoms suggests a propensity to low thermal conductivity, which is favorable for thermoelectric applications. Our density functional theory calculations indicate that the semimetallic nature of $Ba_3Si_4$ is the origin for the rather large thermopower. $Ba_3Si_4$ shows high potential for a thermoelectric material with a Seebeck coefficient as large as $-120$ μV $K^{-1}$ for 0.2 electrons/formula units through the substitution of Ba by appropriate cations, such as Y.



## Introduction

Thermoelectricity is one of the material properties harvested for renewable energy production over recent years. The potential of a material for thermoelectric (TE) applications can be determined through the dimensionless figure of merit $ZT = \alpha^2\sigma T/\kappa$ where $\alpha$ is the Seebeck coefficient, $\sigma$ is the electrical conductivity, $T$ is the absolute temperature and $\kappa$ is the thermal conductivity.[1] Doped semiconductors and semimetals meet the electronic prerequisite for optimum power factors $PF = \alpha^2\sigma$. The best standard thermoelectric materials are alloys based on $Bi_2Te_3$, PbTe or $Si_{1-x}Ge_x$ with a $ZT$ of about 1. There are as well promising antimonides and chalcogenides which have been found during the last few decades.[1–3] However, most of these materials are made of toxic and rare chemical elements, hence the intense search for new TE compounds is based on abundant and nontoxic elements.

Alkaline-earth silicides form a class of promising TE materials which have been studied for their large variety of crystal structures and electronic ground states. Several types of semiconductors such as orthorhombic $BaSi_2$, $A_2Si$ (A = Ca, Sr, Ba), $Ca_3Si_4$ and $Ca_{14}Si_{19}$ have attracted attention for photovoltaic and thermoelectric applications.[4–9] Type I clathrates $A_8Si_{46}$ (A = Ba, Sr) and type IX clathrates are cage compounds that can be synthesized at high-pressure and high temperature with superconducting ground states and interesting dynamic properties of the guest atom A.[10] When Si atoms are substituted by Ga or Al atoms, the thermoelectric properties increase strongly with a $ZT$ reaching 0.87 at 870 K for $BaGa_{16}Si_{30}$.[11,12]

Recently, first-principles calculations have shown that $Ba_3Si_4$[13] and cubic $SrSi_2$[14] as well as cubic CoSi[15] are topological semimetals with many potential applications such as in the thermoelectric field. This was indeed confirmed for $SrSi_2$ with the best $ZT$ obtained at room temperature among the silicide alloys.[16] In particular, in the absence of spin–orbit coupling (SOC), there are three types of topological elements in $Ba_3Si_4$ generated by the crossings of three bands: a nodal-chain network, intersecting nodal rings and triple points linked by a nodal line.[13] In the presence of SOC, the intersecting nodal rings are gapped and the triple points split into two Dirac points because of band splitting with one of the crossing points gapped.[13] As these splitting energies are small, it has been suggested that these topological features can be observed experimentally.[13] In more recent DFT studies of topological materials, Zhang *et al.* found that $Ba_3Si_4$ belongs to the general class of high symmetry point semimetals when the spin–orbit coupling is not taken into account. The topological points are split during SOC.[17,18] Tang *et al.* also predicted some band crossing in the semimetal $Ba_3Si_4$[19] whereas Vergniory *et al.* found that $Ba_3Si_4$ has an integer linear combination of elementary band representations that could be compatible with either fragile or trivial topology but without a fragile band in this case.[20–23]

$Ba_3Si_4$ crystallizes in the tetragonal space group $P4_2/mnm$ (no. 136). It has a complex crystal structure with the inclusion of quasi-isolated butterfly-shaped $Si_4^{6-}$ Zintl anions. They are formed by two three-fold bonded Si(1) atoms, two two-fold

[a] *ICGM, Univ Montpellier, CNRS, ENSCM, Montpellier, France. E-mail: romain.viennois@umontpellier.fr*
[b] *Institut Laue Langevin, 71 avenue des Martyrs, F-38042 Grenoble, France*
[c] *ICMMO, CNRS, UMR 8182, Université Paris Saclay, F-91405 Orsay, France*

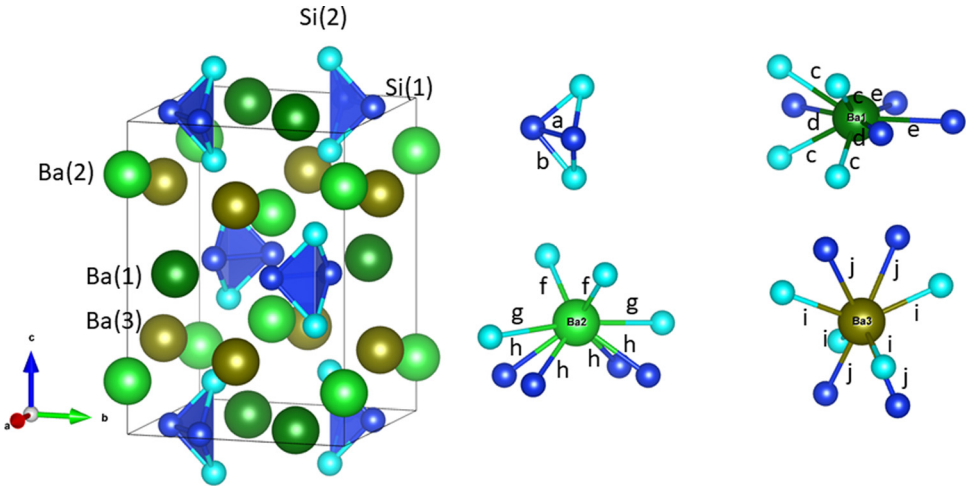


Fig. 1 Left: the crystal structure of tetragonal $Ba_3Si_4$ from the experimental data of ref. 26. Small and large spheres represent Si and Ba atoms, respectively. Different Wyckoff positions are labeled and disclosed by different colors; light blue and dark blue for Si and Si–Si bonds, respectively, and varying green colors for Ba sites.[28] Right: the four different local structural motifs forming the $Ba_3Si_4$ compound. The same color scheme is applied. Interatomic distances are labeled *a*–*j* and correspond to *a* = 2.4183 Å, *b* = 2.4254 Å, *c* = 3.5761 Å, *d* = 3.7061 Å, *e* = 3.7163 Å, *f* = 3.2584 Å, *g* = 3.6177 Å, *h* = 3.3598 Å, *i* = 3.3088 Å and *j* = 3.5174 Å.

bonded Si(2) atoms and heavy Ba atoms[24–26] (see the crystal structure in Fig. 1). This structural complexity makes it a good candidate for a low thermal conductivity material. $Ba_3Si_4$ can be seen as a Zintl compound such as $(Ba^{2+})_3Si_4^{6-}$, but as indicated above, it is semimetallic and not semiconducting. Hydrogenation of $Ba_3Si_4$ could transform these butterfly $Si_4^{6-}$ anions into tetrahedron-shaped $Si_4^{4-}$ polyanions with hydrogen atoms in interstitial sites.[27] To date, the physical properties of $Ba_3Si_4$ have been hardly studied.[26] In the present work, we report the electronic and thermoelectric properties of $Ba_3Si_4$ computed using density functional theory (DFT) and Boltzmann transport theory, and its lattice dynamics studied *via* inelastic neutron scattering (INS) experiments and DFT methods, which we refer to as DFT-LD hereafter.

## Computation and experimental details

DFT calculations were based on projector augmented wave (PAW) pseudopotentials and the Perdew-Burke-Ernzerhof (PBE) exchange–correlation functional using the Vienna *ab initio* Simulation Package (VASP).[29–31] For all calculations, an energy cut-off of 350 eV was applied. The force convergence was $10^{-3}$ eV Å$^{-1}$ with an energy convergence of $10^{-10}$ eV. We applied a grid of 11 × 11 × 11 *k* points for this calculation. The calculated tetragonal lattice parameters are *a* = 8.5829 Å and *c* = 11.9549 Å and slightly larger than the experimental values *a* = 8.5233 Å and *c* = 11.8322 Å.[26] The calculated atom fractional coordinates listed in Table 1 agree very well with the experimental data.[26]

The electronic density of states and the thermoelectric properties were calculated using a grid with 25 × 25 × 25 *k*-points. The electron localization function (ELF) was calculated following the description by Becke and Edgecombe.[32] The thermoelectric properties were calculated with the BoltzTrap program in the constant relaxation time $\tau$ approximation within a rigid band model.[33] For the lattice dynamics calculations, we used the supercell method implemented in the PHONON program.[34] The calculations were performed in a 2 × 2 × 2 supercell with a grid of 5 × 5 × 5 *k* points.

Table 1 Fractional coordinates and isotropic atomic displacement parameters $U_{iso}$ of different atoms derived from the DFT-based lattice dynamics calculations at 300 K and compared to the experimental data obtained at room temperature by single-crystal XRD by Aydemir *et al.*[26]

| Atom | Site | *x* | *y* | *z* | $U_{iso}$ (Å$^2$) | |
|---|---|---|---|---|---|---|
| Ba(1) | 4f | 0.33598 | *x* | 0 | 0.01639 | DFT |
| | | 0.33515 | *x* | 0 | 0.01466 | XRD[26] |
| Ba(2) | 4e | 0 | 0 | 0.16922 | 0.01137 | DFT |
| | | 0 | 0 | 0.16963 | 0.01031 | XRD[26] |
| Ba(3) | 4d | 0 | $\frac{1}{2}$ | $\frac{1}{4}$ | 0.01355 | DFT |
| | | 0 | $\frac{1}{2}$ | $\frac{1}{4}$ | 0.01212 | XRD[26] |
| Si(1) | 8i | 0.8996 | 0.30034 | 0 | 0.01282 | DFT |
| | | 0.90055 | 0.30007 | 0 | 0.01134 | XRD[26] |
| Si(2) | 8j | 0.19924 | *x* | 0.35597 | 0.01547 | DFT |
| | | 0.20077 | *x* | 0.35403 | 0.01359 | XRD[26] |

The formation enthalpies $H_{form}$ of pure and doped $Ba_3Si_4$ were calculated as the difference between the ground state energy *E* of the compounds $Ba_{12}Si_{16}$, $Ba_{11}YSi_{16}$ and $Ba_{12}Si_{15}Al$, obtained by DFT calculations, and of the ground states of the monatomic Ba, Y, Si, and Al crystals.

$$E_{form}(Ba_{11}MSi_{16}) = \frac{E(Ba_{11}MSi_{16}) - 11E(Ba) - E(M) - 16E(Si)}{28} \quad (1)$$

$$E_{form}(Ba_{12}Si_{15}M) = \frac{E(Ba_{12}Si_{15}M) - 12E(Ba) - E(M) - 15E(Si)}{28} \quad (2)$$

The insertion energy $E_{in}$ was obtained from the formation

 

energies of the substituted compound and of $Ba_{12}Si_{16}$ as

$$E_{in} = \frac{E_{form}(Ba_{11}MSi_{16}) - E_{form}(Ba_{12}Si_{16})}{64} \quad (3)$$

$$E_{in} = \frac{E_{form}(Ba_{12}Si_{15}M) - E_{form}(Ba_{12}Si_{16})}{64} \quad (4)$$

Having carried out a full relaxation of the supercell, we observed a small distortion in the *ab* plane of the crystal lifting its tetragonal symmetry. In a second computation approach, the tetragonal symmetry was enforced to the *a* and *b* cell parameters while keeping the *c* parameter and volume fixed to the values of the prior full relaxation run. The differences in $H_{form}$ and $E_{in}$ between the two relaxation runs are less than 1.5 meV per atom and 0.05 eV, respectively. They are of the order of the precision of the calculations and thus do not change the main conclusions drawn for the doping of $Ba_3Si_4$.

The $Ba_3Si_4$ samples were synthesized using an arc melting furnace from Ba (98.5%) and Si (99.999%) pieces in stoichiometric amounts under an Ar atmosphere. Powders were analyzed using X-ray diffraction (Philips X'PERT, Cu-$K_\alpha$ radiation using an accelerated detector PW 3050/60 at 45 kV, 30 mA settings). When ground to powder, the sample is sensitive to moisture, so the powders were prepared using an Ar glovebox and embedded in vacuum grease. The XRD pattern was simulated using Powdercell[35] and the comparison with the experimental data show that almost all Bragg peaks can be assigned to $Ba_3Si_4$. Three small peaks are identified to be due to BaSi[36] (see Fig. 2).

Raman scattering experiments have been performed using a T64000 spectrometer from Horiba–Jobin Yvon in backscattering geometry and a triple-monochromator configuration using a 488 nm laser. The triple-monochromator configuration enabled us to study all low-energy Raman modes of $Ba_3Si_4$. The error in Raman frequencies is about 2 $cm^{-1}$. The Raman experiments were performed on small single-crystal pieces, which are much less sensitive to moisture than powder.

Inelastic neutron scattering (INS) experiments were performed using time-of-flight spectrometers IN5 and IN4 at the Institut Laue Langevin in Grenoble, France. Neutron incident wavelengths of 5 Å at IN5 and 1.1 and 1.6 Å at IN4 were applied. After the synthesis, the sample was stored in a glove box under an Ar atmosphere prior to the INS experiments. All INS measurements were carried out in standard cryostats with the sample under a helium atmosphere of 10–20 bars at $T = 300$ K. Standard corrections were applied to the data comprising empty container signal, instrument and frame overlap backgrounds, detector efficiencies and their energy dependence. From the corrected INS spectra, the generalized density of states (GDOS) $G^{exp}(\omega,T)$ was computed within the incoherent approximation.[37,38]

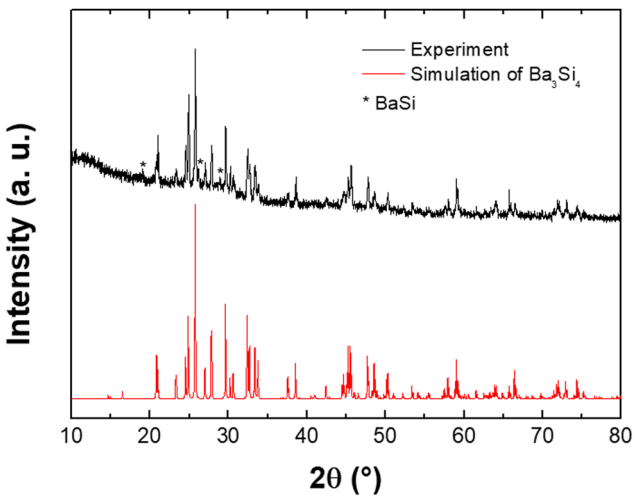


Fig. 2 X-ray diffraction pattern of the $Ba_3Si_4$ sample (top) compared to a simulation (bottom). The asterisks indicate the Bragg peaks of the BaSi compound.

## Electronic and thermoelectric properties

We begin to discuss our results with the electronic structure and thermoelectric properties of $Ba_3Si_4$. We report the electronic band structure and density of states around the Fermi level in Fig. 3. The overlap of the valence and conduction bands around $\Gamma$ and the low value of the electronic density of states at the Fermi level are the characteristics of a semimetallic material and in good agreement with prior calculations.[13,18,23,26,27] Notably, we observe the crossing of the valence and conduction bands close to the Fermi level well corresponding to the different topological features described and analyzed in detail by Cai *et al.*[14] The two peaks in the electronic DOS close to the Fermi level are noted. They correspond to the bottom of the conduction band at −0.045 eV and the top of the valence band at 0.005 eV and signify the overlap between these two bands of 0.05 eV. In Fig. 4, we report the 3D representation of the ELF for ELF = 0.8 and the 2D cross-section through the [001] plane. One can clearly see that the Ba atoms have spherical ELF characteristics of ionic bonding. We also clearly see the attractors of the lone pairs of different Si atoms. When decreasing the ELF to 0.76, the attractors between the different Si atoms appear, indicating that the electrons in covalent Si–Si bonding are much less localized than the electrons in the lone pairs. All these characteristics are typical of Zintl compounds,[39] although here $Ba_3Si_4$ is semimetallic due to the overlap of the highest valence and lowest conduction bands around $\Gamma$.

This semimetallic nature with a low charge carrier concentration suggests the potential for TE applications as in the case of semimetallic CoSi showing good TE properties.[40–42] As seen in the Introduction, both CoSi[15] and $Ba_3Si_4$[13] are topological semimetals although of different nature. It has already been shown[43] that the topology anomalies can give additional contributions to the TE power of the topological metal or semimetal.

In Fig. 5, we report the anisotropy of the electrical conductivity and that of the Seebeck coefficient perpendicular and

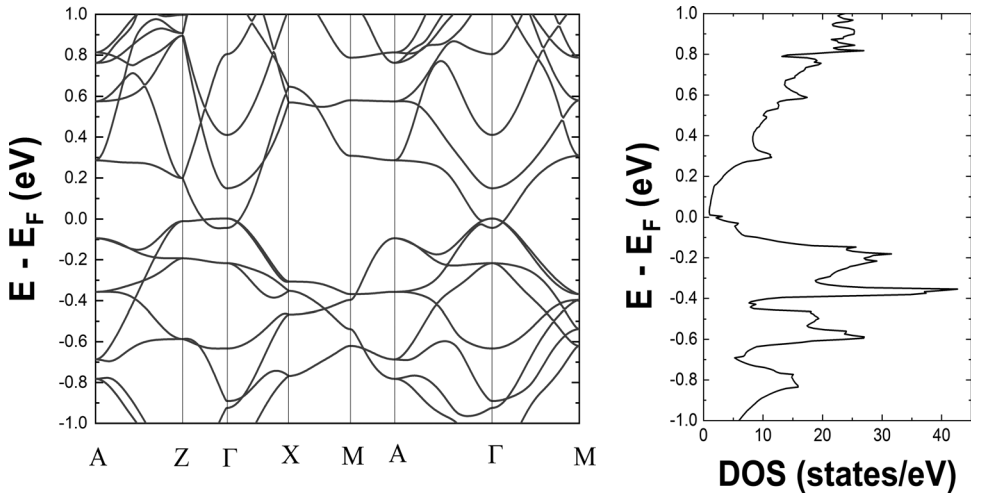


Fig. 3 Left: the electronic band structure and right: the density of states in the vicinity of the Fermi level. The high symmetry points in the Brillouin zone correspond to $\Gamma$ (0,0,0) $A$ (1/2,1/2,1/2), $Z$ (0,0,1/2), $X$ (1/2,0,0) and $M$ (1/2, 1/2,0).

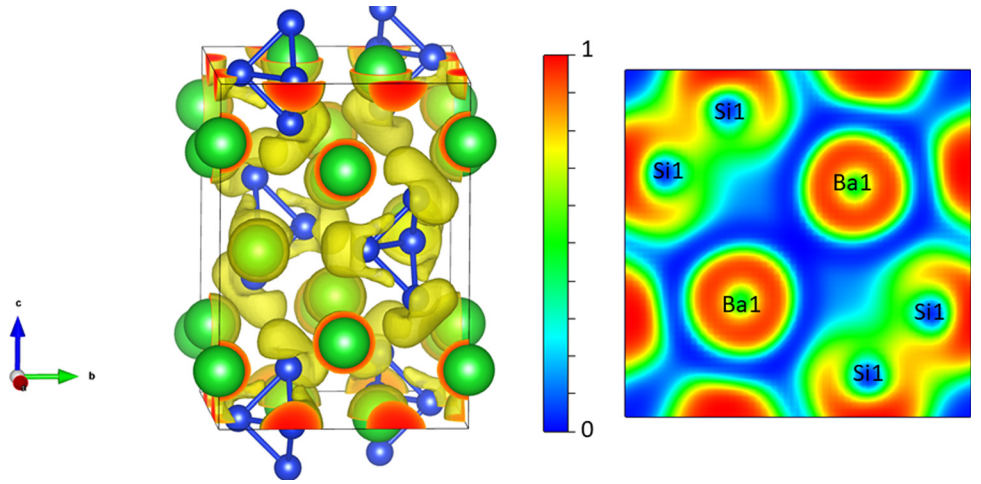


Fig. 4 Left: 3D representation of the ELF isosurface with ELF = 0.8. Right: 2D cross section through the [0 0 1] plane of the ELF.

parallel to the $c$ axis and the average Seebeck coefficient which is computed as $\alpha_{av} = (2\sigma_{xx}\alpha + \sigma_{zz}\alpha_{zz})/3\sigma_{av}$ (with $\sigma_{av} = (2\sigma_{xx} + \sigma_{zz})/3$). In Fig. 5(a)–(c), they are reported as a function of the chemical potential $\mu$ and compared with the variation of the electronic DOS. One can see that close to $\mu = 0$ eV, the absolute value of the Seebeck coefficient is larger for the valence band than for the conduction band and this is the opposite concerning the electrical conductivity. For better insight into the variation of the thermoelectric properties with doping, we report the Seebeck coefficient and the electrical conductivity as a function of the charge carrier concentration $N$ in Fig. 5(d)–(f). The positive $N$ value corresponds to hole doping whereas the negative $N$ value marks electron doping. The anisotropy of the Seebeck coefficient varies with the charge carrier concentration. For electron doping with $-0.1 < N < 0$ e per fu and for hole doping with $0.05 < N < 0.7$ h per fu, the absolute value of the Seebeck coefficient is significantly larger in the $c$ direction. The electrical conductivity is always larger in the $ab$ plane than that in the $c$ direction for electron doping $-1 < N < 0$ e per fu and for hole doping with $0 < N < 0.45$ h per fu. These results can be explained by the much larger dispersion of the conduction and valence bands in the $\Gamma X$ and $\Gamma M$ directions than those in the $\Gamma Z$ direction, resulting in a much smaller effective mass m* and larger delocalization of the charge carriers in the ab plane than those in the $c$ direction. Thus, this explains naturally the anisotropy of the electrical conductivity and the Seebeck coefficient as in a first approximation $\sigma \propto 1/m^*$ and $\alpha \propto m^*$.

In Fig. 6, we report the average Seebeck coefficient $\alpha_{av}$ and the power factor PF = $\alpha_{av}^2\sigma_{av}/\tau$ as a function of the charge carrier concentration at different temperatures. For electron doping, one can see that the absolute value of the Seebeck coefficient has a maximum for $N = -0.1$ e per fu, increases from 300 K to 600 K and becomes almost temperature independent upon further heating. The best absolute values of the Seebeck coefficients in the case of electron doping are comparable with those of CoSi which has a $ZT$ of about 0.15–0.2 above 600 K[40–42]

 

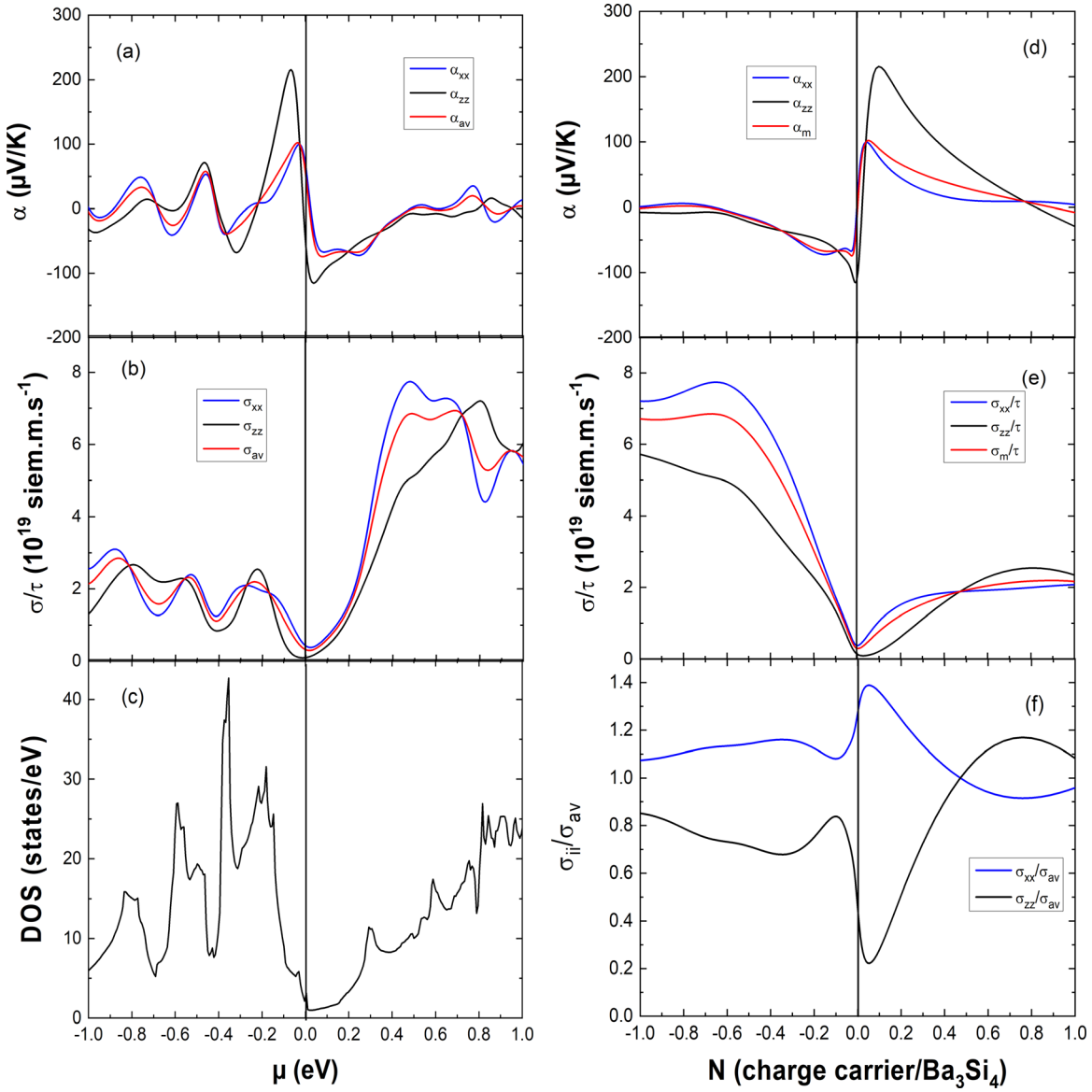


Fig. 5 Left: DFT-computed (a) average $\alpha_{av}$ and directional $\alpha_{xx}$ and $\alpha_{zz}$ Seebeck coefficients, (b) average $\sigma_{av}/\tau$ and directional $\sigma_{xx}/\tau$ and $\sigma_{zz}/\tau$ electrical conductivities and (c) electronic DOS in the function of the chemical potential $\mu$ at 300 K. Right: the DFT-computed effect of the charge carrier concentration $N$ at 300 K on (d) the average $\alpha_{av}$ and directional $\alpha_{xx}$ and $\alpha_{zz}$ Seebeck coefficients, (e) the average $\sigma_{av}/\tau$ and directional $\sigma_{xx}/\tau$ and $\sigma_{zz}/\tau$ electrical conductivities and (f) on the ratio of the directional and average electrical conductivities $\sigma_{xx}/\sigma_{av}$ and $\sigma_{zz}/\sigma_{av}$. The negative and positive $N$ values correspond to electron doping and hole doping, respectively.

or of the bad metal $LaFe_4Sb_{12}$[44] with $ZT$ as large as 0.7 at 800 K.[45]

For hole doping, one can see that the maximum of the Seebeck coefficient shifts to higher charge carrier concentrations and lower values with increasing temperature. At 300 K, a similar maximum power factor is found for both electron doping and hole doping for about $N = -0.2$ e per fu and $N = 0.1$ h per fu, respectively. However, for hole doping, at a higher temperature, the power factor decreases marking hole doping an inept approach for good TE performance. In the case of electron doping, the power factor increases upon heating by a factor 3 and becomes almost constant above 900 K, still for $N = -0.2$ e per fu. This is a very promising result for TE applications. A possibly viable way of accomplishing the doping requirements for the best TE performance of $Ba_3Si_4$ could be the substitution of Ba by Y for electron doping (optimum electron doping for $Ba_{2.8}Y_{0.2}Si_4$) and by Al for hole doping (optimum hole doping for $Ba_3Si_{3.9}Al_{0.1}$). So far, it has not been clarified what maximum doping values the solubilities of Y and Al allow to reach. An accurate study of the Ba–Y–Si and Ba–Al–Si phase diagrams is needed. Note that the high sensitivity of $Ba_3Si_4$ to air and moisture will need specific care to characterize its thermoelectric properties.

Here, we have calculated the formation enthalpies $H_{form}$ of pure and Al- and Y- doped $Ba_3Si_4$ as well as the insertion energies $E_{in}$ of Al and Y in $Ba_3Si_4$ in order to determine if these

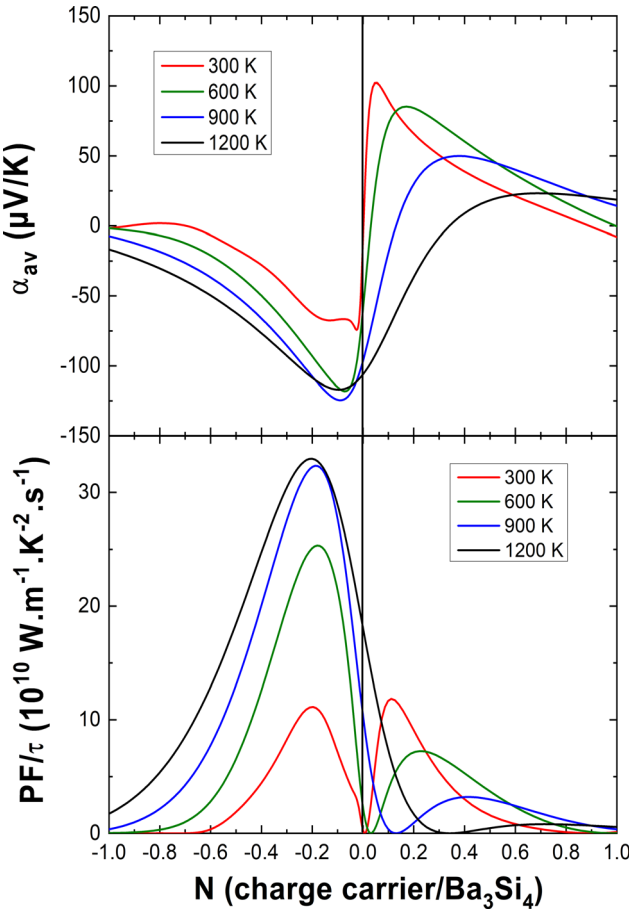


Fig. 6 Top: the DFT-computed effect of the charge carrier concentration $N$ and of temperature $T$ on the average Seebeck coefficient. Bottom: the corresponding average power factor $PF/\tau = \alpha_{av}^2\sigma_{av}/\tau$ (bottom).

elements are soluble in $Ba_3Si_4$ and on which sites the substitutions take place. The results are shown in Table 2.

Y-doping should decrease significantly the lattice volume and modify very differently the lattice parameters depending on which the Ba site is substituted. Y insertion in Ba2 sites decreases the formation enthalpy $H_{form}$ and leads to a negative insertion energy $E_{in}$. We conclude that Y should be soluble in $Ba_3Si_4$ and substitute preferentially on the Ba2 sites. Note that the insertion in Ba3 and Ba2 sites is progressively less favorable. In comparison, Al substitution is energetically less favorable and increases slightly the lattice volume. The low values of insertion energies $E_{in}$ suggest however the possibility of substitution at high temperatures when configurational entropic and vibrational contributions play a stronger role.

Table 2 Lattice parameters, atomic volume $V_{at}$, formation enthalpies $H_{form}$ and insertion energies $E_{in}$ of pure and doped $Ba_3Si_4$ derived from DFT calculations

| Compositions | Substitution site | $a$ (Å) | $c$ (Å) | $V_{at}$ (Å$^3$) | $H_{form}$ (eV/atom) | $E_{in}$ (eV) |
|---|---|---|---|---|---|---|
| $Ba_3Si_4$ | | 8.5829 | 11.9549 | 31.45 | −0.407 | |
| $Ba_{11}YSi_{16}$ | Ba1 | 8.4711 | 11.9557 | 30.64 | −0.375 | 0.89 |
| $Ba_{11}YSi_{16}$ | Ba2 | 8.544 | 11.564 | 30.15 | −0.41 | −0.1 |
| $Ba_{11}YSi_{16}$ | Ba3 | 8.5043 | 11.6874 | 30.19 | −0.397 | 0.28 |
| $Ba_{12}Si_{15}Al$ | Si1 | 8.5645 | 12.0375 | 31.53 | −0.392 | 0.41 |
| $Ba_{12}Si_{15}Al$ | Si2 | 8.6828 | 11.8232 | 31.76 | −0.394 | 0.36 |

## Lattice dynamics and thermodynamic properties

In $Ba_3Si_4$, there are 28 atoms in the primitive cell and thus 84 different vibrational modes. The decomposition in irreducible representation is as follows:

$$\Gamma_{opt} = 6\,A_{1g} \oplus 4\,A_{2g} \oplus 5\,B_{1g} \oplus 7\,B_{2g} \oplus 10\,E_g \oplus 3\,A_{1u} \oplus 5\,A_{2u} \oplus 5\,B_{1u} \oplus 2\,B_{2u} \oplus 12\,E_u \quad \text{and} \quad \Gamma_{ac} = A_{2u} \oplus E_u$$

There are 28 Raman-active modes with $A_{1g}$, $B_{1g}$, $B_{2g}$ and $E_g$ symmetries and 17 Infrared-active excitations of $A_{2u}$ and $E_u$ symmetries.

All DFT-computed Gamma point frequencies and their symmetries are reported in Table 3. A comparison of the calculated Raman modes with two experimental Raman spectra is shown in Fig. 7 and enables some mode symmetry assignments. The results of the assignment are detailed in Table 4. Note that in many cases several modes correspond to the Raman lines observed in our experiments.

We report in Fig. 8 the phonon dispersion curves and the total and atom-projected phonon DOS of $Ba_3Si_4$ obtained from DFT-based lattice dynamics calculations. The phonon properties of $Ba_3Si_4$ show some very particular features which are worth highlighting. A dispersive character of the phonon system, which one might think of being the characteristic of acoustic phonons, is only obvious below 5 meV, despite the highest energy excitations reach almost 55 meV. Consequently, above 5 meV, all vibrational eigen-modes are highly localized. The strongly localized phonons form five clearly and extensively separated phonon bands. The lowest energy band ranges up to about 12.5 meV and cannot be discriminated from the acoustic regime. The second excitation band covers a wide energy range from 14 to 22 meV. It is followed by an extended excitation gap up to 35 meV where a narrower excitation band begins reaching out to 39 meV. The remaining localized eigen-modes form two almost singular lines in the phonon DOS centered at about 47 and 52.5 meV and are once more separated by large excitation gaps of 7 and 5 meV, respectively.

In addition to this striking localization and extensive gap characteristics of the phonon system, the vibrational amplitudes of the Ba and Si atoms are highly decoupled. This is best viewed in the atom-projected DOS on the right-hand side of Fig. 8. Note that the excitation band of the lowest energy ($<$12.5 meV) is basically dominated by the Ba vibrations deep into the acoustic regime. From the second excitation band, the vibrations are dominated by the Si amplitudes with no noticeable Ba contribution to the 3 high-energy phonon bands. There is as well a clear difference in the partial contributions from the 3 non-equivalent Ba sites, with Ba(1) eigen-vectors showing a preference for lower energies than Ba(2) and Ba(3). The preferences can be quantified by the mean energy $\langle E \rangle$ of the partial contributions resulting to

 

Table 3 Gamma point eigen-frequencies and their symmetries as derived from DFT calculations

| Symmetry | Frequency ($cm^{-1}$) |
|---|---|
| $A_{1g}$ | 76, 84.9, 150, 177.3, 284.9, 423 |
| $A_{2g}$ | 65.5, 141.8, 154.5, 312.8 |
| $B_{1g}$ | 52.7, 64.3, 135.6, 148.5, 313.1 |
| $B_{2g}$ | 70.4, 84.7, 105.3, 138.3, 154, 287.1, 420 |
| $E_g$ | 51.1, 64.5, 68.6, 80, 89.5, 128.5, 151.6, 162.4, 295.8, 374.9 |
| $A_{1u}$ | 71.8, 163, 306.1 |
| $A_{2u}$ | 77.8, 79.5, 131.9, 155.3, 373.6 |
| $B_{1u}$ | 53.4, 90.9, 145.1, 155, 377.4 |
| $B_{2u}$ | 162.4, 306.9 |
| $E_u$ | 54.7, 68.7, 70.7, 71.5, 95, 129.9, 134, 152.5, 168.9, 292.5, 306.9, 425.4 |

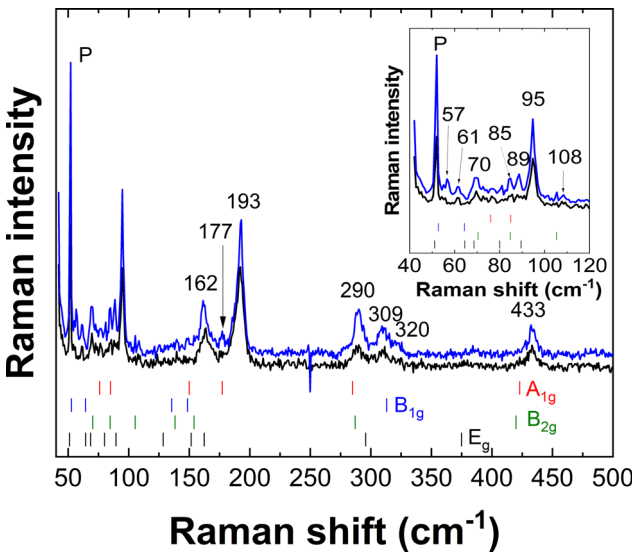


Fig. 7 Experimental Raman spectra from two different zones of the $Ba_3Si_4$ sample. The tick bars correspond to the eigen-frequencies of the Raman-active modes derived from DFT calculations. Inset: Zoom at a spectrum with energies lower than 120 $cm^{-1}$.

Table 4 Measured Raman mode frequencies in $cm^{-1}$ and their symmetries as identified through lattice dynamics DFT calculations

| Frequency/$cm^{-1}$ | Symmetry (DFT) |
|---|---|
| 57 | $E_g$ (51.1) |
| 61 | $B_{1g}$ (52.7) |
| 70 | ? |
| 85 | $E_g$ (80) |
| 89 | $B_{2g}$ (84.7) + $A_{1g}$ (84.9) |
| 95 | $E_g$ (89.5) |
| 108 | $B_{2g}$ (105.3) |
| 162 | $B_{1g}$ (148.5) + $A_{1g}$ (150) + $E_g$ (11.6) + $B_{2g}$ (154) |
| 177 | $E_g$ (162.4) |
| 193 | $A_{1g}$ (177.3) |
| 290 | $A_{1g}$ (284.9) + $B_{2g}$ (287.1) |
| 309 | $E_g$ (295.8) |
| 320 | $B_{1g}$ (313.1) |
| 433 | $B_{2g}$ (420) + $A_{1g}$ (423) |

8.27 meV for Ba(1), 9.54 meV for Ba(3) and 10.67 meV for Ba(2). The sequence of increasing mean energies of Ba(1), Ba(3) and Ba(2) suggests this order for their bonding strength which correlates well with reciprocal mean distances of 3.6425 Å for Ba(1)–Si, 3.413 Å for Ba(3)–Si and 3.399 Å for Ba(2)–Si.[26] See Fig. 1 for more details on the local structures. As we will show hereafter, the validity of the differences in the Ba-projected DOS is confirmed by diffraction results and can be further discriminated by the lattice direction. This holds equally for the properties of the two non-equivalent Si atoms. Although a difference is not clearly evident in the DOS presentation of Fig. 8, it is noticeable in the mean energy values of 29.19 meV for Si(1) and 26.15 meV for Si(2).

However, before discussing the effect of the partial contributions in more detail, let us establish the validity of the particular DOS features by a comparison with the INS experimental data. The contrast maps of the dynamic structure factor $S(Q,E)$ measured at IN4 with an incident neutron wavelength of 1.6 Å at 1.5, 150 and 300 K are shown in Fig. 9. In Fig. 10, we compile the computed generalized densities of states (GDOS) from all IN4 and IN5 data as well as the neutron weighted DOS derived from DFT-based lattice dynamics and broadened for the spectrometer energy resolution.

From the powder-averaged signal of the dynamic structure factor $S(Q,E)$ shown in Fig. 9, the dispersive character of the monitored vibrational modes is clearly obvious for intensities up to the mode gap centered around 15 meV. The bands of acoustic phonons emanating from strong Bragg reflections at zero energy along $E$ up to about 10 meV and high-intensity regions localized in $Q$ highlight the collective character of the sampled excitations. Excitations above the mode gap show a reduced variation upon $Q$ and $E$ as deduced before from the computed phonon dispersion shown in Fig. 8. The increasing intensity towards high $Q$ and with mounting temperatures reflects the basic dependence of phonon form-factors on $Q$ and thermal occupation, respectively.

The temperature corrected and phase space averaged GDOS signals shown in Fig. 10 are in very good agreement with the DFT-LD results. Note that, for convenience, the resolution-broadened DOS has been normalized to 21 phonon modes and the GDOS recorded at 150 K was compared with the DOS for peak amplitudes in the low-E region. We highlight that within the resolution of the experimental setup, all measured phonon peaks are reproduced and the characteristic energies matched with high precision by the computed DOS. This is in particular the case for the Si-dominated high-E modes. In the Ba-dominated low-E region, the two strong peaks are somehow

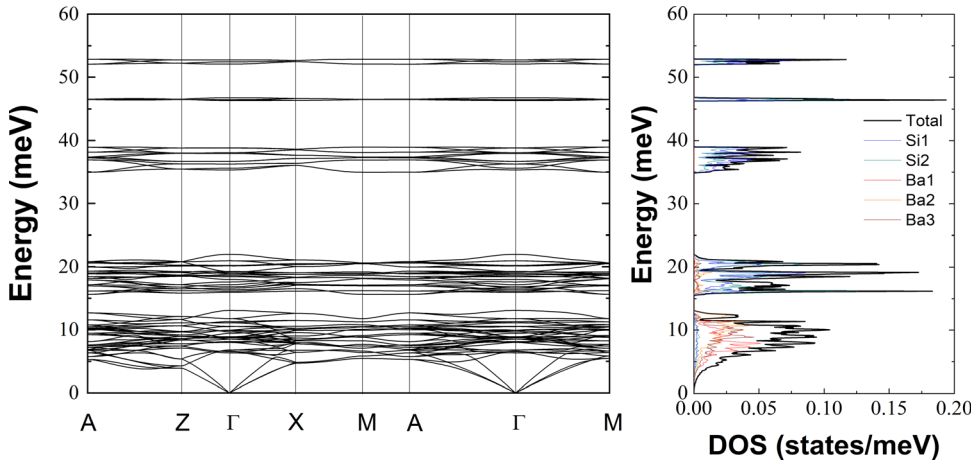


Fig. 8 Left: phonon dispersion curves derived from DFT-based lattice dynamics calculations. The indicated *k* points *Γ*, *A*, *Z*, *X*, and *M* correspond to the respective high symmetry points (0,0,0), (1/2,1/2,1/2), (0,0,1/2), (1/2,0,0), and (1/2, 1/2,0) of the crystal's Brillouin zone. Right: the total and atom-projected phonon density of states (DOS). Different contributions are disclosed by different colors specified in the figure.

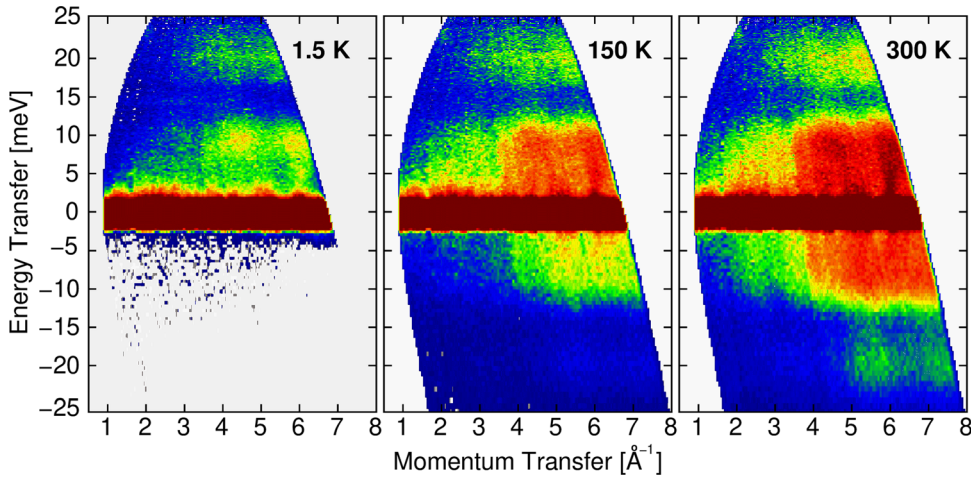


Fig. 9 Contrast maps of S(*Q*,*E*) recorded at IN4 with $\lambda$ = 1.6 Å at the indicated temperatures. The positive and negative energies characterize the Stokes and anti-Stokes lines, respectively.

sharper and shifted to lower energies by about 10% in the DOS. This indicates that the Ba–Si coupling is slightly underestimated by the DFT calculations. A similar effect has been found for Ba–Si clathrates[46] and a stronger underestimation of the Ba–Ge coupling has been found in Ba–Ge clathrates[47,48] having applied PBE exchange–correlation functionals.

We may locate these Ba-dominated low-E peaks at 10 and 20 meV in the GDOS data. This result is temperature independent as evidenced by the higher resolution data shown on the right of Fig. 10. The progressive reduction of the intensity in the IN4 data upon heating is a result of the Debye–Waller factor. The difference in the amplitudes of the two peaks recorded at 300 K in the IN5 data with respect to the IN4 signal is a result of the different phase spaces covered by the two instruments and experimental setups.

To highlight the significance of the differences in the atom-projected DOS as shown in Fig. 8, we compare in Fig. 11 the isotropic thermal displacement parameters $U_{iso}(T)$ derived from our DFT-LD data with experimental results taken at room temperature by Aydemir *et al.*[26] The excellent correspondence of the DFT-LD and experimental results is noted. As expected and pointed out above, the weak underestimation of the Ba–Si coupling in the low-energy region of the DOS is demonstrated here by a slight shift of the DFT-LD data towards higher values. The subtle differences of the Si(1) and Si(2) specific dynamics which are less clear in Fig. 8 become obvious here and follow compellingly the experimental data as the three Ba-specific $U_{iso}(T)$ do. Thus, the two-fold bonded Si(2) experiences higher displacement parameters than the three-fold bonded Si(1) in line with their specific mean energies $<E>$ reported above.

The excellent agreement between experiment and calculations can be further tracked down to the level of anisotropic displacement parameters $U_{ij}$. They are listed in Table 5. Note that the sequence of $U_{ij}$ values derived from experiment is fully

 

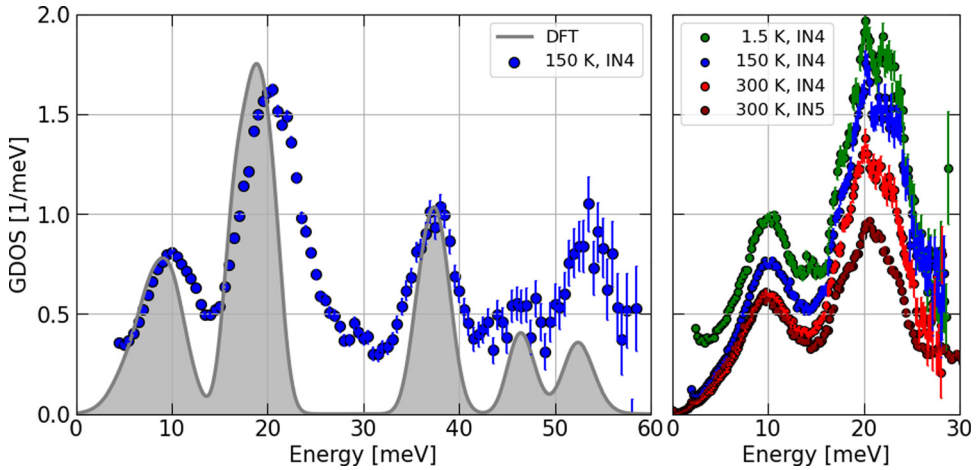


Fig. 10 GDOS of $Ba_3Si_4$ from INS experiments at different temperatures (symbols) and neutron weighted DOS from DFT calculations (gray shaded areas). Left: INS data recorded at IN4 (Stokes line) at 150 K with $\lambda$ = 1.1 Å. The DFT results are broadened to account approximatively for the energy resolution of the experimental setup. Right: data recorded at IN4 (Stokes line) with $\lambda$ = 1.6 Å and IN5 (anti-Stokes line) with $\lambda$ = 5 Å at the indicated temperatures. See text for details.

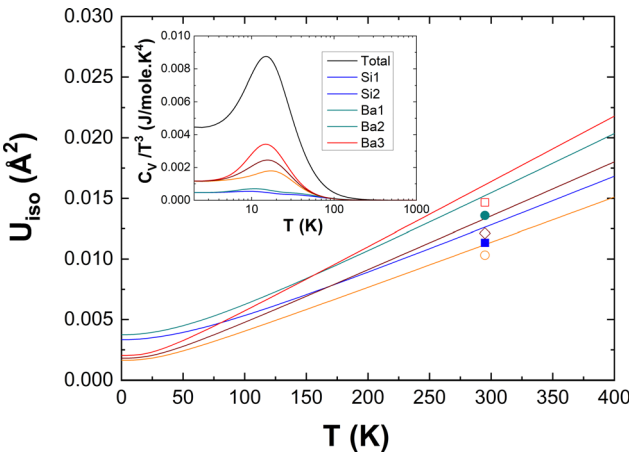


Fig. 11 Isotropic atomic displacement parameters $U_{iso}$ from DFT calculations (solid lines) compared to experimental values[26] (symbols). Inset: Debye plot $C_V/T^3$ as a function of temperature.

respected by our computation data for diagonal and off-diagonal elements. Our data affirm the weak anisotropies in $U_{ij}$ of all atoms conjectured from experiments. They confirm as well the variation in the bond strength of the Ba atoms. In contrast to Ba(1) and Ba(3) which experience a stronger bonds along the $z$ direction than in the $x$–$y$ plane, Ba(2) is stronger bonded in the $x$–$y$ plane than along the $z$ direction.

Finally, the corresponding heat capacity data in a Debye plot ($C_V/T^3$ *vs.* $T$) are reported in the inset of Fig. 11. As expected from the observed peak around 10 meV in the DOS and GDOS, $C_V/T^3$ features a peak at about 15 K on the top of a Debye plateau. The atom-specific characteristics are obvious here by two features. There is a clear variation of intensities and a less evident variation of the peaks' positions. Their behavior is comprehensible on a qualitative basis within the basic models of Einstein and Debye taking into account some characteristic energies such as the mean energies $\langle E \rangle$ calculated above. At low $T$, the atom-specific peak positions scale with $\langle E \rangle$ and the peak intensities are expected to follow $\sim \exp(-\langle E \rangle / k_B T)$ within the Einstein model. An equivalent explanation is offered by the Debye model for the intensities of the Debye plateau. They are supposed to scale as $1/\langle E \rangle^3$ at low $T$. Thus, the differences in $C_V/T^3$ of the three symmetry-non-equivalent Ba atoms and the rather Debye-like $C_V/T^3$ of the Si atoms are anticipated.

Table 5 Anisotropic atomic displacement parameters $U_{ij}$ from DFT-LD calculations at 300 K compared to room temperature single-crystal XRD data by Aydemir *et al.*[26]

| Atom | Site | $U_{xx}$ (Å$^2$) | $U_{yy}$ (Å$^2$) | $U_{zz}$ (Å$^2$) | $U_{yz} = U_{xz}$ (Å$^2$) | $U_{xy}$ (Å$^2$) | |
|---|---|---|---|---|---|---|---|
| Ba(1) | 4f | 0.01511 | $U_{xx}$ | 0.01894 | 0.00002 | −0.00035 | DFT |
| | | 0.01296 | $U_{xx}$ | 0.01805 | 0 | −0.00047 | XRD[26] |
| Ba(2) | 4e | 0.01221 | $U_{xx}$ | 0.00969 | 0.00002 | 0.00058 | DFT |
| | | 0.01111 | $U_{xx}$ | 0.00871 | 0 | 0.00067 | XRD[26] |
| Ba(3) | 4d | 0.01306 | $U_{xx}$ | 0.01453 | 0.00002 | 0.00000 | DFT |
| | | 0.01186 | $U_{xx}$ | 0.01264 | 0 | 0 | XRD[26] |
| Si(1) | 8i | 0.01148 | 0.01448 | 0.01251 | 0.00004 | −0.00122 | DFT |
| | | 0.01005 | 0.01263 | 0.01135 | 0 | −0.00111 | XRD[26] |
| Si(2) | 8j | 0.01515 | $U_{xx}$ | 0.0161 | −0.0038 | 0.00102 | DFT |
| | | 0.01303 | $U_{xx}$ | 0.01472 | −0.00326 | 0.00064 | XRD[26] |

## Conclusion

In the present paper, we have investigated the electronic, thermoelectric, and phonon properties of the topological semimetal $Ba_3Si_4$. The bonding properties of $Ba_3Si_4$ are the characteristic of Zintl phases despite the semimetallic nature of the compound. This semimetallic nature results in a rather high Seebeck coefficient which is a prerequisite for good thermoelectric properties as found in some other silicides with similar characteristics. We believe that Y doping on Ba sites could make $Ba_3Si_4$ a potential thermoelectric material, if high enough doping concentrations could be achieved.

The lattice dynamics of the material has been studied by Raman and inelastic neutron scattering experiments as well as *ab initio* lattice dynamics calculations. Good agreement of the experimental data with the *ab initio* results is observed. The presence of low-energy optical modes with dominating Ba participation is another prerequisite for the good thermoelectric performance of the material. In this case, the localization of vibrational modes in the energy domain of heat carrying acoustic phonons is supposed to open up an appreciable number of additional scattering channels for the heat carriers and thus reduce the lattice thermal conductivity. The high number of 84 eigen-modes out of which 81 are localized is a result of the complex structure of $Ba_3Si_4$ and points at an enhanced phase–space volume for Umklapp-scattering processes.

The very good agreement of the lattice dynamics calculations with the experimental results up to the level of anisotropic thermal displacement parameters underlines the accuracy of our *ab initio* computed data. This agreement strengthens our confidence in the validity of the computed electronic properties and thus in the charge carrier and temperature dependence of the electrical conductivity, the Seebeck coefficient and the power factor. It is a solid guide for the experimental work to follow.

## Conflicts of interest

The authors have no conflicts of interest to declare.

## References

1 G. J. Snyder and E. S. Toberer, Complex thermoelectric materials, *Nat. Mater.*, 2008, **7**, 105–114.
2 C. Han, Q. Sun, Z. Li and S. X. Dou, Thermoelectric enhancement of different kinds of metal chalcogenides, *Adv. Energy Mater.*, 2016, **6**, 1600498.
3 T. Zhu, Y. Liu, C. Fu, J. P. Heremans, G. J. Snyder and X. Zhao, Compromise and synergy in high-efficiency thermoelectric materials, *Adv. Mater.*, 2017, **29**, 1605884.
4 W. Du, M. Suzuno, M. A. Khan, K. Toh, M. Baba, K. Nakamura, K. Toko, N. Usami and T. Suemasu, Improved photoresponsivity of semiconducting $BaSi_2$epitaxial films grown on a tunnel junction for thin-film solar cells, *Appl. Phys. Lett.*, 2012, **100**, 152114.
5 K. Hashimoto, K. Kurosaki, Y. Imamura, H. Muta and S. Yamanaka, Thermoelectric properties of $BaSi_2$, $SrSi_2$, and LaSi, *J. Appl. Phys.*, 2007, **102**, 063703.
6 S. A. Dotsenko, D. V. Fomin, K. N. Galkin, D. L. Goroshko and N. G. Galkin, Growth, optical and electrical properties of Ca2Si film grown on Si(111) and $Mg_2Si$/Si(111) substrates, *Phys. Proc*, 2011, **11**, 95–98.
7 C. Wen, T. Nonomura, A. Kato, Y. Kenichi, H. Udono, K. Isobe, M. Otake, Y. Kubota, T. Nakamura, Y. Hayakawa and H. Tatsuoka, Electrical properties of $Ca_2Si$ sintered compact synthesized by spark plasma sintering, *Phys. Procedia*, 2011, **11**, 106–109.
8 S. Yabuuchi, Y. Kurosaki, A. Nishide, N. Fukutani and J. Hayakawa, First-principles study on thermoelectric transport properties of $Ca_3Si_4$, *Phys. Rev. Mater.*, 2017, **1**, 045405.
9 A. Moll, R. Viennois, P. Hermet, A. Haidoux, J.-L. Bantignies and M. Beaudhuin, Stability and properties of the friendly environmental Zintl phases: $Ca_3Si_4$ and $Ca_{14}Si_{19}$, *Acta Mater.*, 2017, **125**, 490–497.
10 A. San Miguel and P. Toulemonde, High-pressure properties of group IV clathrates, *High Press. Res.*, 2005, **25**, 159–185.
11 V. L. Kuznetsov, L. A. Kuznetsov, A. E. Kalliazin and D. M. Rowe, Preparation and thermoelectric properties of $A^{II}{}_8B^{III}{}_{16}B^{IV}{}_{30}$ clathrate compounds, *J. Appl. Phys.*, 2000, **87**, 7871–7875.
12 J. H. Roudebush, E. S. Toberer, H. Hope, G. J. Snyder and S. M. Kauzlarich, Crystal structure, characterization and thermoelectric properties of the type-I clathrate $Ba_{8-y}Sr_yAl_{14}Si_{32}$ ($0.6 \leq y \leq 1.3$) prepared by aluminium flux, *J. Solid State Chem.*, 2011, **184**, 1176–1185.
13 J. Cai, Y. Xie, P.-Y. Chang, H.-S. Kim and Y. Chen, Nodal-chain network, intersecting nodal rings and triple points coexisting in nonsymmorphic $Ba_3Si_4$, *Phys. Chem. Chem. Phys.*, 2018, **20**, 21177–21183.
14 S.-M. Huang, *et al.*, New type of Weyl semimetal with quadratic double Weyl fermions, *Proc. Nat. Acad. Sci. U. S. A.*, 2016, **113**, 1180–1185.
15 D. A. Pshenay-Severin, Y. V. Ivanov, A. A. Burkov and A. T. Burkov, Band structure and unconventional electronic topology of CoSi, *J. Phys.: Condens. Matter*, 2018, **30**, 135501.
16 C. S. Lue, M. D. Chou, N. Kaurav, Y. T. Chung and Y. K. Kuo, Enhancement in the thermoelectric performance by Y substitution on $SrSi_2$, *Appl. Phys. Lett.*, 2009, **94**, 192105.
17 T. Zhang, Y. Jiang, Z. Song, H. Huang, Y. He, Z. Fang, H. Weng and C. Fang, Catalogue of topological electronic materials, *Nature*, 2019, **566**, 475–479.
18 **https://materiae.iphy.ac.cn/#/**.
19 F. Tang, H.-C. Po, A. Vishwanath and X. Wan, Comprehensive search for topological materials using symmetry indicators, *Nature*, 2019, **566**, 486–490.
20 B. Bradlyn, L. Elcoro, J. Cano, M. G. Vergniory, Z. Wang, C. Felser, M. L. Aroyo and B. A. Bernevig, Toplogical quantum chemistry, *Nature*, 2017, **547**, 298–305.
21 M. G. Vergniory, L. Elcoro, C. Felser, N. Regnault, B. A. Bernevig and Z. Wang, A complete catalogue of high-quality topological materials, *Nature*, 2019, **566**, 480–485.
22 M. G. Vergniory, B. J. Wieder, L. Elcoro, S. S. P. Parkin, C. Felser, B. A. Bernevig and N. Regnault, All topological bands of all nonmagnetic stoichiometric materials, *Science*, 2022, **376**, eabg9094.
23 **https://www.topologicalquantumchemistry.com**.
24 B. Eisenmann, K. H. Janzon, H. Schäfer and A. Weiss, Zur kenntnis von $Ba_3Si_4$, *Z. Naturforsch., B*, 1969, **24**, 457–458.
25 M. Pani and A. Palenzona, The phase diagram of the Ba-Si system, *J. Alloys Compd.*, 2008, **454**, L1–L2.
26 U. Aydemir, A. Ormeci, H. Borrmann, B. Böhme, F. Zürcher, B. Uslu, T. Goebel, W. Schnelle, P. Simon, W. Carillo-Cabrera, F. Haarmann, M. Baitinger, R. Nesper, H. G. von

 

Schnering and Y. Grin, The metallic Zintl phase $Ba_3Si_4$: synthesis, crystal structure, chemical bonding, and physical properties, *Z. Anorg. Allg. Chem.*, 2008, **634**, 1651–1661.

27 V. F. Kranak, D. E. Benson, L. Wollmann, M. Mesgar, S. Shafeie, J. Grins and U. Häussermann, Hydrogenous Zintl phase $Ba_3Si_4H_x$ ($x$ = 1–2): transforming $Si_4$ "butterfly" anions into tetrahedral moieties, *Inorg. Chem.*, 2015, **54**, 756–764.

28 K. Momma and F. Izumi, VESTA 3 for three-dimensional visualization of crystal, volumetric and morphology data, *J. Appl. Cryst.*, 2011, **44**, 1272–1276.

29 G. Kresse and J. Furthmüller, Efficient iterative schemes for *ab initio* total-energy calculations using a plane-wave basis set, *Phys. Rev. B: Condens. Matter Mater. Phys.*, 1996, **54**, 11169–11186.

30 G. Kresse and D. Joubert, From ultrasoft pseudopotentials to the projector augmented-wave method, *Phys. Rev. B: Condens. Matter Mater. Phys.*, 1999, **59**, 1758–1775.

31 J. P. Perdew, K. Burke and M. Erzenhof, Generalized gradient approximation made simple, *Phys. Rev. Lett.*, 1996, **77**, 3865–3868.

32 A. D. Becke and K. E. Edgecombe, A simple measure of electron localization in atomic and molecular systems, *J. Chem. Phys.*, 1990, **92**, 5397–5403.

33 G. K. H. Madsen and D. J. Singh, BoltzTraP. A code for calculating band-structure dependent quantities, *Comput. Phys. Commun.*, 2006, **175**, 67–71.

34 K. Parlinski, Z.-Q. Li and Y. Kawazoe, First-principles determination of the soft mode in cubic $ZrO_2$, *Phys. Rev. Lett.*, 1997, **78**, 4063–4066.

35 W. Krauss and G. Nolez, POWDERCELL – a program for the representation and manipulation of crystal structures and calculation of the resulting X-ray powder patterns, *J. Appl. Cryst.*, 1996, **29**, 301–303.

36 A. Currao, J. Curda and R. Nesper, Kann man die arten von Zintl-anionen steuern? Variationen über das thema $Si^{2-}$ im system Sr/Mg/Si, *Z. Anorg. Allg. Chem.*, 1996, **622**, 85–94.

37 M. M. Bredov, B. A. Kotov, N. M. Okuneva, V. S. Oskotskii and A. L. Shakh-Budagov, Possibility of measuring thermal vibrations spectrum G(W) using coherent inelastic neutron scattering from a polycrystalline sample, *Phys. Solid State*, 1967, **9**, 214.

38 V. S. Oskotskii, Measurement of phonon distribution function in polycrystalline materials using coherent scattering of slow neutrons into a solid angle, *Phys. Solid State*, 1967, **9**, 420.

39 A. Sakai, F. Ishii, Y. Onose, Y. Tomioka, S. Yotsuhashi, H. Adachi, N. Nagaosa and Y. Tokura, Thermoelectric power oin transition-metal monosilicides, *J. Phys. Soc. Jpn.*, 2007, **76**, 093601.

40 R. Viennois, X. Tao, P. Jund and J.-C. Tedenac, Stability and thermoelectric properties of transition-metal silicides, *J. Electron. Mater.*, 2011, **40**, 597–600.

41 M. Longhin, R. Viennois, D. Ravot, J.-J. Robin, B. Villeroy, J.-B. Vaney, C. Candolfi, B. Lenoir and P. Papet, *J. Electron. Mater.*, 2015, **44**, 1963–1966.

42 D. A. Pshenay-Severin, Y. V. Ivanov, A. A. Burkov and A. T. Burkov, Band structure and unconventional electronic topology of CoSi, *J. Phys.: Condens. Matter*, 2018, **30**, 135501.

43 R. Lundgren, P. Laurell and G. A. Fiete, Thermoelectric properties of Weyl and Dirac semimetals, *Phys. Rev. B: Condens. Matter Mater. Phys.*, 2014, **90**, 165115.

44 R. Viennois, L. Girard, D. Ravot, S. Paschen, S. Charar, A. Mauger, P. Haen and J.-C. Tedenac, Thermoelectric properties of (Ce,La)$Fe_4Sb_{12}$ skutterudites under a magnetic field, *Phys. Rev. B: Condens. Matter Mater. Phys.*, 2009, **80**, 155109.

45 P. F. Qiu, J. Yang, R. H. Liu, X. Shi, X. Y. Huang, G. J. Snyder, W. Zhang and L. D. Chen, High-temperature electrical and thermal transport properties of fully filled skutterudites $RFe_4Sb_{12}$ (R = Ca, Sr, Ba, La, Ce, Pr, Nd, Eu, and Yb), *J. Appl. Phys.*, 2011, **109**, 063713.

46 R. Viennois, M. M. Koza, R. Debord, P. Toulemonde, H. Mutka and S. Pailhès, Anisotropic low-energy vibrational modes as an effect of cage geometry in the binary baryum silicon clathrate $Ba_{24}Si_{100}$, *Phys. Rev. B*, 2020, **101**, 224302.

47 M. M. Koza, M. R. Johnson, H. Mutka, M. Rotter, N. Nasir, A. Grytsiv and P. Rogl, Vibrational dynamics of the type-I clathrate Ba8ZnxGe$_{46-x-y\square\ y}$ ($x$ = 0, 2, 4, 6, 8), *Phys. Rev. B: Condens. Matter Mater. Phys.*, 2010, **82**, 214301.

48 R. Viennois, M. Beaudhuin and M. M. Koza, Strong renormalization of Ba vibrations in thermoelectric type-IX clathrate $Ba_{24}Ge_{100}$, *Phys. Rev. B*, 2022, **105**, 054314.